Oscillation of a floating body in a viscous fluid

Ronald W. YEUNG and P. ANANTHAKRISHNAN
Department of Naval Architecture and Offshore Engineering, University of California at Berkeley, CA 94720, USA

Abstract. The nonlinear viscous-flow problem associated with the heaving motion of a two-dimensional floating cylinder is considered. It is formulated as an initial-boundary-value problem in primitive variables and solved using a finite-difference method based on boundary-fitted coordinates. A fractional-step procedure is used to advance the solution in time. As a case study, results are obtained for a rectangular cylinder oscillating at a Reynolds number of 10^3. The nonlinear viscous forces are compared with those of linear potential theory. An assessment on the importance of viscous and nonlinear effects is made. The solution technique is sufficiently robust that extensions to consider other single and coupled modes of motion are possible.

1. Introduction

Many investigations have been carried out in the past to understand the fluid-dynamics processes associated with oscillating bodies in a free surface. From a practical viewpoint, such investigations are significant since the results are used for estimating wave loads experienced by offshore structures and for predicting motion response of ocean vehicles. Classical first-order potential-theory results are known to be reasonably accurate for the case of small-amplitude motion in the intermediate range of wave frequencies (see Wehausen [27]). Second-order analyses (e.g. Potash [20], Sclavounos [21]) indicate that nonlinear effects are important in the high-frequency regime.

A more direct approach to the fully nonlinear potential-flow problem is by time domain analysis. Several variants of a mixed Eulerian–Lagrangian boundary-integral method, originated by Longuet–Higgins and Cokelet [18], have been developed (e.g. Vinje and Brevig [25], Baker et al. [2], Cooker et al. [9]) for obtaining nonlinear inviscid solutions to wave-body interaction problems. This mixed formulation can also be implemented using finite-difference methods (see e.g. Telste [24], Yeung and Wu [28]). Telste [24], who considered the heave oscillation of a surface-piercing cylinder, was able to demonstrate the importance of nonlinear effects at high frequency and of large-amplitudes of oscillation.

Despite some known, important effects of viscosity, such as in damping of roll motions, in loads induced by vortex shedding, etc., relatively few cases of viscous-flow analyses have been carried out in this area. Using an extended version of the Marker-and-cell (MAC) method originated by Harlow and Welch [12], Nichols and Hirt [14] computed the hydro-dynamic forces on a surface-piercing cylinder heaving with small amplitudes. More elaborate versions of the MAC method have been continually developed. For example, Miyata et al. [19] solved a wave-diffraction problem using a version called TUMMAC. The computed results in [19], however, showed large deviations in horizontal exciting forces from those of experimental results.

The primary difficulty encountered in tackling viscous-flow problems is that the Navier–Stokes equations are nonlinear with the unknown variables pressure and velocity coupled together. The use of vorticity and stream-function formulation would allow one to decouple

the pressure and velocity fields. However, the procedure can neither be easily extended to the three-dimensional case, nor be used to accommodate stress-type boundary conditions in any straightforward manner.

Viscous-flow problems with free boundaries have further complications. The problem associated with contriving a proper open-boundary condition is nontrivial (see Yeung [29]). Waves of large amplitude often lead to skewed or extreme geometry, imposing rather stringent demand on domain-discretization techniques. Proper discretization is imperative, otherwise boundary conditions cannot be accurately implemented and detail structures such as vorticity generation cannot be effectively resolved. Finally, no completely satisfactory model has yet been devised to model the movement of the contact line (intersection of the body and free surface).

Recently, the authors have completed the development of a numerical method based on boundary-fitted coordinates for solving fully nonlinear viscous free-surface flow problems (see Ananthakrishnan [1]). The solution of the Navier–Stokes equations in primitive variables is based on the fractional-step method originally formulated by Chorin [7], Temam [23] and others. Briefly, an intermediate velocity field (also referred to as the 'auxiliary field') is first computed by neglecting the pressure terms. The pressure field is obtained by solving a Poisson equation. The correctional effects of pressure are then incorporated into the auxiliary field to determine the divergence-free velocity field. Our fractional-step formulation is implemented using a finite-difference method based on boundary-fitted coordinates. A variational formulation involving the concept of a reference space (see Steinberg and Roache [22], Yeung and Ananthakrishnan [31]) is used to generate grids. Previously, using this grid-generation technique in conjunction with the mixed Lagrangian–Eulerian formulation, we were able to obtain highly nonlinear *inviscid-flow* solutions, such as shallow-water breaking waves [30] and wave diffraction over submerged obstacles [32].

In the present work, we use the above finite-difference procedure to solve the nonlinear viscous-flow problem associated with heaving motion of a floating body. Solutions are obtained for a range of physical parameters, including the possibility of large amplitude of body oscillation.

2. Mathematical formulation

Notations and definitions of the problem being studied are described in Fig. 1. A fixed (inertial) coordinate system with the x-axis along the mean water level and the y-axis
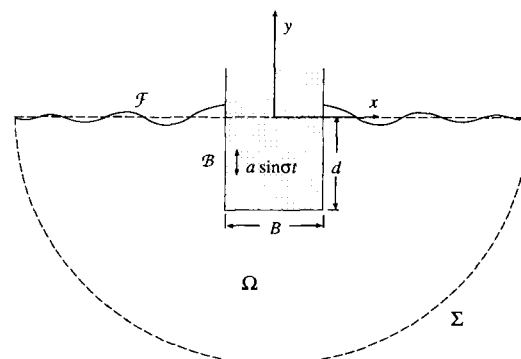

Fig. 1. Cylinder heaving in a viscous fluid, problem definition and notations (in dimensional form).

pointing upwards is chosen. The equilibrium draft of the rectangular body is denoted by d and the beam by B. The amplitude and frequency (in rad/sec) of oscillation are given by a and σ, respectively. The free surface is denoted by $\mathscr{F}$, the body contour by $\mathscr{B}$, and an open boundary by Σ. The kinematic viscosity coefficient of the fluid is denoted by ν, its density by ρ, and the gravitational acceleration by g. The governing equations will be nondimensionalized with respect to B, ρ, and σ. Accordingly, time is scaled by $1/\sigma$, length by B, velocity by σB, pressure by $\rho B^2 \sigma^2$, and force by $\rho B^3 \sigma^2$. We will henceforth adopt this nondimensionalized notation. Where convenient, subscripts followed by a comma (,) will be used to denote partial differentiation with respect to the subscripted variables.

2.1. Field equations

The field equations governing the viscous wave problem are the Navier–Stokes equations:

$$\nabla \cdot \mathbf{u} = 0 \tag{1}$$

and

$$\frac{\partial \mathbf{u}}{\partial t} + (\mathbf{u} \cdot \nabla)\mathbf{u} = -\nabla\left(p + \frac{y}{F_\sigma^2}\right) + \frac{1}{R_\sigma} \nabla^2 \mathbf{u}, \tag{2}$$

which are derived using the conservation laws of mass and momentum, with the fluid being assumed incompressible, homogeneous, and Newtonian. The unknown variables $\mathbf{u} = \mathbf{u}(\mathbf{x}, t) = (u, v)$ and $p(\mathbf{x}, t)$ are the velocity and pressure fields, respectively. As is commonly known, the second term on the left-hand side is associated with convective effects of the fluid and the last term on the right-hand side with diffusion effects of viscosity. In the above equation, R_σ and F_σ are defined by

$$R_\sigma = \frac{\sigma B^2}{\nu}, \tag{3}$$

$$F_\sigma = \sigma\sqrt{\frac{B}{g}}, \tag{4}$$

which will henceforth be referred to as the Reynolds number and as the frequency parameter, respectively.

2.2. Boundary conditions

On $\mathscr{F}$, in the absence of surface tension, continuity of stress vector components along the normal and tangential directions provides the following dynamic conditions:

$$n_i T_{ij} n_j = 0, \tag{5}$$

$$\tau_i T_{ij} n_j = 0, \tag{6}$$

where

$$T_{ij} = -p\delta_{ij} + \frac{1}{R_\sigma} \left\{ \frac{\partial u_i}{\partial x_j} + \frac{\partial u_j}{\partial x_i} \right\} \tag{7}$$

is the stress tensor in the indicial notation. (n_1, n_2) and (τ_1, τ_2) in equations (5) and (6) denote the components of unit normal- and tangential-vectors, respectively.

The unknown elevation of the free surface can be tracked in time by integrating the following Lagrangian description of $\mathcal{F}$

$$\frac{D}{Dt} \mathbf{x} = \mathbf{u} , \tag{8}$$

where D/Dt denotes the material derivative. For non-breaking waves, the following Eulerian description can also be used to advance the free-surface elevation, $y = Y(x, t)$:

$$\frac{\partial Y}{\partial t} = v - u \frac{\partial Y}{\partial x} . \tag{9}$$

The body is forced to heave (vertically) in the form of

$$y_b(t) = y_b(0) + \frac{a}{B} \sin(t) , \quad t \geq 0 , \tag{10}$$

where $y_b(t)$ represents the y-coordinate value of any point fixed to the rigid body. The prescribed motion can be arbitrary, but sinusoidal motion is chosen here merely for illustration. On the body surface $\mathcal{B}$, the appropriate no-flux and no-slip conditions are imposed:

$$u = 0 , \tag{11}$$

$$v = \frac{a}{B} \cos(t) . \tag{12}$$

Approximate conditions are used at the intersection of the body and the free surface to model its movement. Several experimental and theoretical investigations have been devoted solely to examine the precise mechanisms occurring near the contact line (see e.g., Dussan [10], Huh and Mason [15], Koplik et al. [17]), but the findings are still inconclusive. Hence, as an approximation, we find it plausible to assume that the fluid slips freely at the contact line; in other words,

$$\frac{\partial v}{\partial x} = 0 \quad \text{at } \mathcal{B} \cap \mathcal{F} \tag{13}$$

is assumed for computing the y-component of the velocity. The horizontal component of the velocity at $\mathcal{B} \cap \mathcal{F}$ is given by the no-flux condition (11).

Approximate conditions are also used, in the present work, for the closure of the problem at the open boundary Σ. Accordingly, at sufficiently large distance from the body we assume that

$$p = p_{\text{stat}} , \tag{14}$$

where p_{stat} denotes the pressure field of the quiescent fluid (see Grosenbaugh and Yeung [11]

for a similar treatment of an inviscid flow problem). An auxiliary velocity at Σ is determined by first-order spatial extrapolation. A decomposition relation, which is a consequence of the fractional-step procedure, is used to determine the unknown velocity at Σ. Specific details of the fractional-step procedure are given later.

The above open-boundary condition can result in wave reflections when the radiating waves reach Σ. The steady-state, inviscid-fluid dispersion relation of deep-water gravity waves, i.e.

$$\lambda = 2\pi/F_\sigma^2 ,\tag{15}$$

where λ is the nondimensional wavelength, can be used to position the open boundary sufficiently far so that wave reflections occurring at Σ during the course of the simulation are negligibly small. However, transient waves of larger wavelength may reach the boundary Σ sooner.

The field equations together with the given boundary conditions are solved as an *initial-value* problem. The initial data are taken to be those of the static (quiescent) fluid case. The body motion is started impulsively at $t = 0^+$.

2.3. Force calculation

At each instant of discrete time (after solving for the unknowns, namely $\mathbf{u}$, p, and the free-surface elevation, using the above field and boundary equations), the vertical component of the stress vector can be integrated along $\mathcal{B}$ to determine the nondimensional heave force F exerted by the body:

$$F = -\int_{\mathcal{B}} T_{2j} n_j \, \mathrm{d}s = -\int_{\mathcal{B}} \left\{ \frac{1}{R_\sigma} \left(\frac{\partial u}{\partial y} + \frac{\partial v}{\partial x} \right) n_1 + \left(-p + \frac{2}{R_\sigma} \frac{\partial v}{\partial y} \right) n_2 \right\} \mathrm{d}s ,\tag{16}$$

where $\mathrm{d}s$ is the differential (arc-length). One can also compute the contributions of each term in the above equation in order to estimate viscous- and pressure-term contributions (bearing in mind, however, that pressure is affected by viscosity also). Thus, the viscous shear-stress component F_s of the heave force can be written as

$$F_s = -\frac{1}{R_\sigma} \int_{\mathcal{B}} \left(\frac{\partial u}{\partial y} + \frac{\partial v}{\partial x} \right) n_1 \, \mathrm{d}s,\tag{17}$$

and the normal viscous-stress component F_n as

$$F_n = -\frac{2}{R_\sigma} \int_{\mathcal{B}} \frac{\partial v}{\partial y} n_2 \, \mathrm{d}s .\tag{18}$$

Subtracting the static-pressure component $(-y/F_\sigma^2)$ from the total pressure p, we can compute the dynamic-pressure force F_p as

$$F_p = \int_{\mathcal{B}} \left(p + \frac{y}{F_\sigma^2} \right) n_2 \, \mathrm{d}s .\tag{19}$$

Once the velocity field is known, the vorticity field

$$\omega(\mathbf{x}, t) = \frac{\partial v}{\partial x} - \frac{\partial u}{\partial y} \qquad (20)$$

can also be computed.

3. Method of numerical solution

As shown in Fig. 2, the physical space $(x, y; t)$ is mapped to a computational space $(\xi, \eta; T)$ so that the governing equations can be solved in a uniform rectangular mesh. The mapping introduces the following transformation relations

$$\partial_{,x} = \frac{1}{J_1} \{ y_{,\eta} \partial_{,\xi} - y_{,\xi} \partial_{,\eta} \} , \qquad (21)$$

$$\partial_{,y} = \frac{1}{J_1} \{ -x_{,\eta} \partial_{,\xi} + x_{,\xi} \partial_{,\eta} \} , \qquad (22)$$

$$\partial_{,t} = \partial_{,T} - \frac{x_{,T}}{J_1} \{ y_{,\eta} \partial_{,\xi} - y_{,\xi} \partial_{,\eta} \} - \frac{y_{,T}}{J_1} \{ -x_{,\eta} \partial_{,\xi} + x_{,\xi} \partial_{,\eta} \} , \qquad (23)$$

where

$$J_1 = x_{,\xi} y_{,\eta} - x_{,\eta} y_{,\xi} \qquad (24)$$

is the Jacobian of the transformation of $(x, y; t)$ to $(\xi, \eta; T)$. Similarly, one can show, as an example, that the Laplace operator in $(x, y; t)$ space when transformed to $(\xi, \eta; T)$ space becomes

$$\partial_{,xx} + \partial_{,yy} = A \partial_{,\xi\xi} - 2B \partial_{,\xi\eta} + C \partial_{,\eta\eta} + E \partial_{,\xi} + F \partial_{,\eta} , \qquad (25)$$

Physical Space
(x,y)

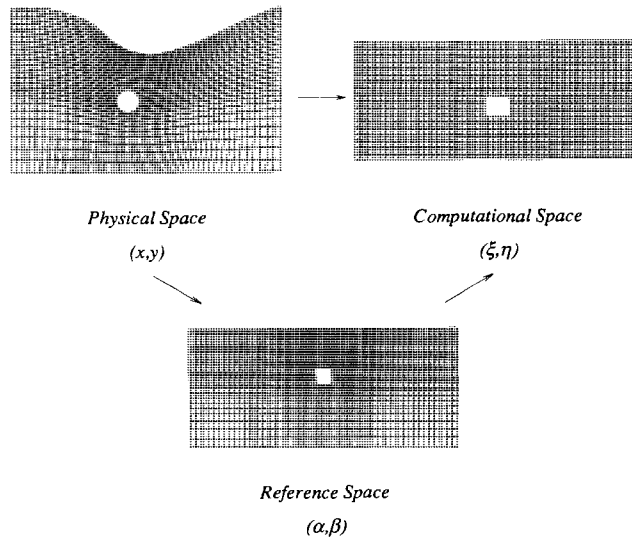Computational Space
(ξ,η)

Reference Space
(α,β)

Fig. 2. Grid generation using reference space.

where

$$A = \frac{x_{,\eta}^2 + y_{,\eta}^2}{J_1^2} , \qquad B = \frac{x_{,\xi}x_{,\eta} + y_{,\xi}y_{,\eta}}{J_1^2} , \qquad C = \frac{x_{,\xi}^2 + y_{,\xi}^2}{J_1^2} ,$$

$$E = \xi_{,xx} + \xi_{,yy} , \qquad F = \eta_{,xx} + \eta_{,yy} .$$

These relations will be used to transform the flow equations, given in Section 2, to the computational space.

3.1. Boundary-fitted coordinates

A grid-generation procedure developed earlier (see Yeung and Ananthakrishnan [31]) has also been used in the present work to implement the coordinate mapping. This is based on a variational formulation (see Brackbill and Saltzman [6]) in conjunction with the notion of a reference space introduced by Steinberg and Roache [22]. The crux of the procedure is that a geometrically-similar intermediate space (α, β) is first discretized, and its properties are then transferred to the physical mesh. This is illustrated in Fig. 2, which is taken from Yeung and Vaidhyanathan [32]. The intermediate space is geometrically simpler than the physical space (see Fig. 2) so that it can be discretized easily, for example, by using simple algebraic relations. The intermediate space is also discretized in such a way that its grid properties such as cell-area distribution and coordinate spacings are also the ones desired in the physical space. For instance, the present problem requires finer resolution of the region near the body and the free surface so that viscosity effects can be accurately resolved. The desired grid properties, that are first achieved in the intermediate-space, are then transferable to the physical mesh by *minimizing* the following functionals:

$$I_s^*(\xi, \eta) = \iint_\Omega \mathrm{d}x\,\mathrm{d}y\, |\nabla_{x,y}\xi|^2 + |\nabla_{x,y}\eta|^2 - \iint_\Omega \mathrm{d}\alpha\,\mathrm{d}\beta\, |\nabla_{\alpha,\beta}\xi|^2 + |\nabla_{\alpha,\beta}\eta|^2 , \tag{26}$$

$$I_c^*(\xi, \eta) = \iint_\Omega \mathrm{d}x\,\mathrm{d}y\, J_2 , \tag{27}$$

$$I_o^*(\xi, \eta) = \iint_\Omega \mathrm{d}x\,\mathrm{d}y\, \{\nabla_{x,y}\xi \cdot \nabla_{x,y}\eta\}^2 J_1^3 , \tag{28}$$

where the subscripts s, c, and o on the left-hand side represent the grid properties, viz. smoothness, cell-area, and orthogonality, respectively. Equation (26) is a measure of the difference, in coordinate spacings, between the physical and the reference spaces. The term J_2 in equation (27) denotes the Jacobian of the mapping of the physical space onto the reference space $(J_2 = x_{,\alpha}y_{,\beta} - x_{,\beta}y_{,\alpha})$. Note that equation (28), the orthogonality functional, corresponds to the direct mapping of $(x, y; t)$ to $(\xi, \eta; T)$ given originally by Brackbill and Saltzman [6]. We do not use the reference space to specify the angular properties of the coordinates. This is because it is preferable to have orthogonal or nearly orthogonal grids for accurate implementation of Neumann-type boundary conditions.

The field equations corresponding to the functionals (26) to (28) are given below:

Smoothness

$$\theta_1 x_{,\xi\xi} - 2\kappa_1 x_{,\xi\eta} + \sigma_1 x_{,\eta\eta} = -\frac{J_1}{J_3^2} \{(\beta_{,\eta}\chi - \alpha_{,\eta}\mu)x_{,\xi} + (-\beta_{,\xi}\chi + \alpha_{,\xi}\mu)x_{,\eta}\} , \tag{29}$$

$$\theta_1 y_{,\xi\xi} - 2\kappa_1 y_{,\xi\eta} + \sigma_1 y_{,\eta\eta} = -\frac{J_1}{J_3^2} \{(\beta_{,\eta}\chi - \alpha_{,\eta}\mu)y_{,\xi} + (-\beta_{,\xi}\chi + \alpha_{,\xi}\mu)y_{,\eta}\} , \tag{30}$$

where

$$\chi = \theta_3 \alpha_{,\xi\xi} - 2\kappa_3 \alpha_{,\xi\eta} + \sigma_3 \alpha_{,\eta\eta} , \qquad \mu = \theta_3 \beta_{,\xi\xi} - 2\kappa_3 \beta_{,\xi\eta} + \sigma_3 \beta_{,\eta\eta} .$$

The coefficients in the above equations are given by

$$\theta_1 = x_{,\eta}^2 + y_{,\eta}^2 , \qquad \kappa_1 = x_{,\xi}x_{,\eta} + y_{,\xi}y_{,\eta} , \qquad \sigma_1 = x_{,\xi}^2 + y_{,\xi}^2 ,$$

$$\theta_3 = \alpha_{,\eta}^2 + \beta_{,\eta}^2 , \qquad \kappa_3 = \alpha_{,\xi}\alpha_{,\eta} + \beta_{,\xi}\beta_{,\eta} , \qquad \sigma_3 = \alpha_{,\xi}^2 + \beta_{,\xi}^2 ,$$

and $J_3 \ (= \alpha_{,\xi}\beta_{,\eta} - \alpha_{,\eta}\beta_{,\xi})$ is the Jacobian of the mapping of the reference space to the computational space.

Cell-area distribution

$$\frac{2}{J_3^2} \{b_{v1}x_{,\xi\xi} + b_{v2}x_{,\xi\eta} + b_{v3}x_{,\eta\eta} + a_{v1}y_{,\xi\xi} + a_{v2}y_{,\xi\eta} + a_{v3}y_{,\eta\eta}\} = -J_1^2 \frac{\partial}{\partial x}\left(\frac{1}{J_3^2}\right) , \tag{31}$$

$$\frac{2}{J_3^2} \{a_{v1}x_{,\xi\xi} + a_{v2}x_{,\xi\eta} + a_{v3}x_{,\eta\eta} + c_{v1}y_{,\xi\xi} + c_{v2}y_{,\xi\eta} + c_{v3}y_{,\eta\eta}\} = -J_1^2 \frac{\partial}{\partial y}\left(\frac{1}{J_3^2}\right) , \tag{32}$$

where

$$a_{v1} = -x_{,\eta}y_{,\eta} , \qquad b_{v1} = y_{,\eta}^2 , \qquad c_{v1} = x_{,\eta}^2 ,$$

$$a_{v2} = x_{,\xi}y_{,\eta} + x_{,\eta}y_{,\xi} , \qquad b_{v2} = -2y_{,\xi}y_{,\eta} , \qquad c_{v2} = -2x_{,\xi}x_{,\eta} ,$$

$$a_{v3} = -x_{,\xi}y_{,\xi} , \qquad b_{v3} = y_{,\xi}^2 , \qquad c_{v3} = x_{,\xi}^2 .$$

Orthogonality

$$b_{o1}x_{,\xi\xi} + b_{o2}x_{,\xi\eta} + b_{o3}x_{,\eta\eta} + a_{o1}y_{,\xi\xi} + a_{o2}y_{,\xi\eta} + a_{o3}y_{,\eta\eta} = 0 , \tag{33}$$

$$a_{o1}x_{,\xi\xi} + a_{o2}x_{,\xi\eta} + a_{o3}x_{,\eta\eta} + c_{o1}y_{,\xi\xi} + c_{o2}y_{,\xi\eta} + c_{o3}y_{,\eta\eta} = 0 , \tag{34}$$

where

$$a_{o1} = x_{,\eta}y_{,\eta} , \qquad b_{o1} = x_{,\eta}^2 , \qquad c_{o1} = y_{,\eta}^2 ,$$

$$a_{o2} = x_{,\xi}y_{,\eta} + x_{,\eta}y_{,\xi} , \qquad b_{o2} = 2(2x_{,\xi}x_{,\eta} + y_{,\xi}y_{,\eta}) , \qquad c_{o2} = 2(2y_{,\xi}y_{,\eta} + x_{,\xi}x_{,\eta}) ,$$

$$a_{o3} = x_{,\xi}y_{,\xi} , \qquad b_{o3} = x_{,\xi}^2 , \qquad c_{o3} = y_{,\xi}^2 .$$

A linear combination of the above field equations taken as

$$\mathcal{L} = \lambda_s \mathcal{E}_s + \lambda_c \mathcal{E}_c + \lambda_o \mathcal{E}_o , \tag{35}$$

where the λs and $\mathcal{E}$s denote respectively, user-specified weighting values and field equations, are solved. The λ values are to be chosen as per the desired levels (or relative importance) of smoothness, cell-area variations and orthogonality, required in a particular problem. At each time step, the field equations for the grid are solved subject to the location of boundary points.

3.2. Fractional-step formulation

The mapping relations (21) to (25) are used to transform the governing equations to the $(\xi, \eta; T)$ space. This is a straightforward workout in calculus but resulting in lengthy expressions. We will therefore, for the purpose of exposition here, present explicitly only the terms in the transformed equations that are essential for the description of the solution method. Remaining terms will be denoted simply by using symbols. Also, for brevity, we retain the notations used in Section 2 to denote differential operators; e.g., the gradient operator ∇ now represents

$$\nabla = (\partial_{,x}, \partial_{,y}) = \left(\frac{1}{J_1} \{ y_{,\eta} \partial_{,\xi} - y_{,\xi} \partial_{,\eta} \}, \frac{1}{J_1} \{ -x_{,\eta} \partial_{,\xi} + x_{,\xi} \partial_{,\eta} \} \right) . \tag{36}$$

The auxiliary velocity field $\mathbf{u}^{aux}$ is first determined by using the momentum equations without the pressure term [8]:

$$(1 - q)\mathbf{u}^{aux} = \delta T \{ \mathbf{u}^n - \mathcal{N}^n + \mathcal{D}^n \} , \tag{37}$$

where the superscript n denote the current instant of discrete time at which solutions are known. $\mathcal{N}^n$ and $\mathcal{D}^n$ are the known terms corresponding to the discretized form of the coordinate-transformed convection and diffusion terms, respectively. The term q on the left-hand side represents the possibility of implicit differencing. In the case of explicit differencing (in time), $q = 0$.

The discretized form of the full *transformed* momentum equation can be written as

$$(1 - q)\mathbf{u}^{n+1} = \delta T \left\{ \mathbf{u}^n - \mathcal{N}^n + \mathcal{D}^n + \nabla \left(p + \frac{y}{F_\sigma^2} \right)^{n+1} \right\} . \tag{38}$$

A comparison of equations (37) and (38) leads to

$$\mathbf{u}^{aux} = \mathbf{u}^{n+1} + (1 - q)^{-1} \delta T \nabla \left(p + \frac{y}{F_\sigma^2} \right)^{n+1} , \tag{39}$$

where

$$\nabla \cdot \mathbf{u}^{n+1} = 0 . \tag{40}$$

In other words, $\mathbf{u}^{aux}$ can be expressed as a direct sum of $\mathbf{u}^{n+1}$ and pressure fields. Equation

(39) can be conveniently rewritten as

$$\mathbf{u}^{\mathrm{aux}} = \mathbf{u}^{n+1} + \nabla\varphi^{n+1} , \tag{41}$$

where

$$\varphi^{n+1} \equiv (1 - q)^{-1} \, \delta T \left(p + \frac{y}{F_\sigma^2} \right)^{n+1} , \tag{42}$$

which should not be mistaken as a velocity potential. Note that equation (42) gives a one-to-one relation between φ and $p + y/F_\sigma^2$ which is dependent on the scheme (i.e., dependent on q).

Once the auxiliary field has been evaluated using equation (37), equation (41) can be used to determine $\nabla\varphi^{n+1}$ and $\mathbf{u}^{n+1}$. The decomposition can be carried out either sequentially or iteratively. Following Kim and Moin [16], we use the following sequential procedure. The Poisson equation for φ

$$\nabla^2\varphi = \nabla \cdot \mathbf{u}^{\mathrm{aux}} , \tag{43}$$

obtained by taking the divergence of equation (41), is solved first for φ (and hence p through equation (42)). The correctional effects are then added to the auxiliary field through equation (41) to obtain $\mathbf{u}^{n+1}$:

$$\mathbf{u}^{n+1} = \mathbf{u}^{\mathrm{aux}} - \nabla\varphi^{n+1} . \tag{44}$$

We will elaborate on the boundary conditions needed for the evaluation of $\mathbf{u}^{\mathrm{aux}}$, φ etc. in the next subsection, after providing a glimpse of some related theoretical aspects in the following paragraph. Details can be found in the cited references.

In problems where the normal component of velocity is zero on the boundary, as in flows bounded by rigid boundaries, one can show using Gauss theorem that $\mathbf{u}^{n+1}$ and $\nabla\varphi$ fields are orthogonal to each other (see Chorin [7]). The orthogonality of the pressure-gradient and the divergence-free-velocity fields, as stated by Bell et al. [5], "effectively eliminates pressure from the system while enforcing 1.2 [the equation of continuity]; in fact, specifying pressure boundary conditions overdetermines the system". Consequently, the decomposition (41) can be expresses as

$$\mathbf{u}^{n+1} = \mathscr{P}\mathbf{u}^{\mathrm{aux}} \tag{45}$$

$$\nabla\varphi^{n+1} = \mathscr{Q}\mathbf{u}^{\mathrm{aux}} = (\mathscr{I} - \mathscr{P})\mathbf{u}^{\mathrm{aux}} , \tag{46}$$

where $\mathscr{P}$ and $\mathscr{Q}$, not explicitly given here, are orthogonal operators which project $\mathbf{u}^{\mathrm{aux}}$ onto the divergence-free $\mathbf{u}^{n+1}$ and $\nabla\varphi$ fields, respectively. The term $\mathscr{I}$ in equation (46) denotes the unit operator. In the case of free-surface flows, however, the divergence-free velocity and pressure-gradient fields are not orthogonal. Hence, operating the *free-surface* Navier–Stokes equations with the projection operator $\mathscr{P}$ would not eliminate the pressure term. The projected pressure term, nevertheless, is determined by the free-surface pressure condition (see Beale [4]). These observations indicate that the velocity boundary conditions on the

body and the stress conditions on the free surface, as given in Section 2, are sufficient for the solution of the pressure and velocity fields.

3.3. Implementation of boundary conditions

In the present work, physical conditions (given in Section 2) and the decomposition relation (41) are taken into account for obtaining numerical boundary conditions for $\mathbf{u}^{aux}$, $(\nabla\varphi)^{n+1}$, and $\mathbf{u}^{n+1}$. Uniform validity of the equation (41) in space is important for obtaining accurate solutions in a consistent manner (see Kim and Moin [16]).

On $\mathscr{B}$, we use

$$\mathbf{u}^{aux} \cdot \mathbf{n} = \mathbf{u}^{n+1} \cdot \mathbf{n} , \tag{47}$$

$$\mathbf{u}^{aux} \cdot \boldsymbol{\tau} \approx \mathbf{u}^{n+1} \cdot \boldsymbol{\tau} + \frac{\partial}{\partial \tau} \left(\varphi^n \right) , \tag{48}$$

(where $\mathbf{n}$ and τ denote unit vectors in the normal and tangential directions, respectively) to specify the values of $\mathbf{u}^{aux}$ on $\mathscr{B}$. Equation (47), in view of equation (41), provides the following homogeneous Neumann condition for φ^{n+1},

$$\frac{\partial}{\partial \mathbf{n}} \left(\varphi^{n+1} \right) = 0 . \tag{49}$$

Note that $\mathbf{u}^{n+1}$ is given by the no-slip conditions (11) and (12). It is determined by the free-slip equations (11) and (13) at the contact points $\mathscr{B} \cap \mathscr{F}$. The location of the body is determined by the forced oscillation, i.e. by equation (10).

On the free surface $\mathscr{F}$, we use an approximation of equation (41) to specify the auxiliary velocity value:

$$\mathbf{u}^{aux} \approx \mathbf{u}^n + \nabla\varphi^n . \tag{50}$$

A two-step predictor-corrector type iterative procedure is applied to the free-surface stress equations for determining $\mathbf{u}^{n+1}$ and φ^{n+1} (see Ananthakrishnan [1] for details). Basically, we begin with the known value of φ from previous instant of time and use it as the Dirichlet condition for the solution of the Poisson equation. Equation (41) is then used to predict $\mathbf{u}^{n+1}$ in the fluid domain. Stress relations, rewritten as Neumann-type relations for u and v in (ξ, η, T) space, are then used to get the first estimate of $\mathbf{u}^{n+1}$ on $\mathscr{F}$. The normal-stress condition with the predicted velocity thus provides the Dirichlet condition for φ at the corrector stage. The remaining steps in the above predictor stage are again repeated in a similar manner for correcting $\mathbf{u}^{n+1}$ and for updating φ^{n+1}. Concurrently, the kinematic condition (8) or (9) is also integrated using the predictor-corrector method to advance the free surface. The above two-step procedures thus require the solution of Poisson equation for φ twice at each instant of time.

At the open boundary Σ, we obtain a Dirichlet condition for φ from the approximation (14), using the scheme-dependent relation (42) between p and φ. The auxiliary-field $\mathbf{u}^{aux}$ is determined by first-order spatial extrapolation. $\mathbf{u}^{n+1}$ is then computed using the decomposition relation (41), i.e. as

$$\mathbf{u}^{n+1} = \mathbf{u}^{aux} - \nabla\varphi^{n+1} . \tag{51}$$

3.4. Numerical schemes

Several schemes to discretize the convection and diffusion terms in the *transformed* momentum equation – e.g. first-order upwind, second-order Adams–Bashforth, forward-time central-space, implicit Crank–Nicholson, etc. – have been considered by Ananthakrishnan [1] in order to evaluate the comparative merits of these schemes applied to viscous-wave problems. In the present work, we use one of the many sets of procedures that have been studied. This procedure consists of using an upwind differencing for the treatment of *coordinate transformed* convection terms and central-differencing for discretizing the diffusion terms; both of these schemes are explicit, and hence $q = 0$ in equation (42).

The Poisson equation (43) is centrally-differenced and solved by a Gaussian elimination based on LU-decomposition; the code requires the storage of (and operations in) only the non-zero band of the coefficient matrix. The grid equations, also centrally differenced, are solved iteratively using mixed over-under relaxation method.

4. Results and discussion

In this section, as a case study, results obtained for a simple section over a range of F_σ and a/B values are presented. A mesh size of (121×41), with coordinates clustered near the body and the free surface, is used for the discretization of the physical space. The value of R_σ is set to be 10^3 for all cases, which is appropriate for the above mesh size. A time-step size of 0.02, which satisfy stability criteria posed by *linear* convection and diffusion problems on the numerical schemes (see Hirsch [13]), is used in all cases. Velocity scales associated with both body velocity and wave celerity are taken into account in satisfying the Courant condition. For grid generation, the physical space with free surface replaced by flat horizontal surface is used as the reference space. This allows discretizing the reference space by simple algebraic interpolation. We remark that this is not a restriction on the grid-generation method. For example, for breaking-wave type problems, grids generated at previous instants of time can effectively be used as the reference mesh (see Yeung and Vaidhyanathan [32]).

4.1. Flow structure

First, in order to illustrate the intricate details of the vorticity/vortex generation around the oscillating body, velocity-vector and vorticity-contour plots corresponding to a typical case of large-amplitude of oscillation $(a/B = 0.2, \ d/B = 0.5, \ F_\sigma = 2.0)$ are shown in Figs 3a–3d. These figures correspond to instants of discrete time that are roughly one-quarter period apart. Figure 3a corresponds to $t = 0.999\,\hat{T}$ (where $\hat{T}$ here denotes the period of oscillation) when the body is ascending. As can be observed, the flow is primarily into the void generated by the upward movement. Note the incipient formation of wake eddies near the sharp edges. Fully developed wake vortices can be seen at a later time during the periodic motion, see e.g. at $t = 1.247\,\hat{T}$ (Fig. 3b). A small asymmetry in the flow field about the centerline $(x = 0)$ can be noticed in the vorticity-contour plot. In this plot, generation of free-surface vorticity, which is rather weak because of small surface curvature, can also be seen. The entire flow picture changes as the body is descending (see Fig. 3c, corresponding to $t = 1.499\,\hat{T}$). The wake eddies that have been formed earlier (during the ascent) undergo
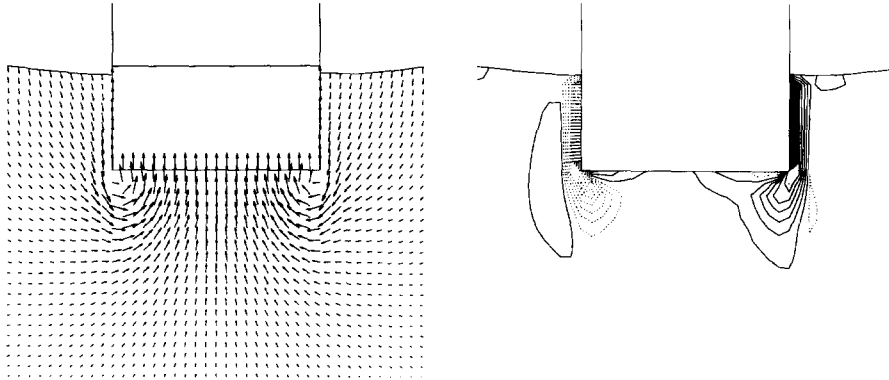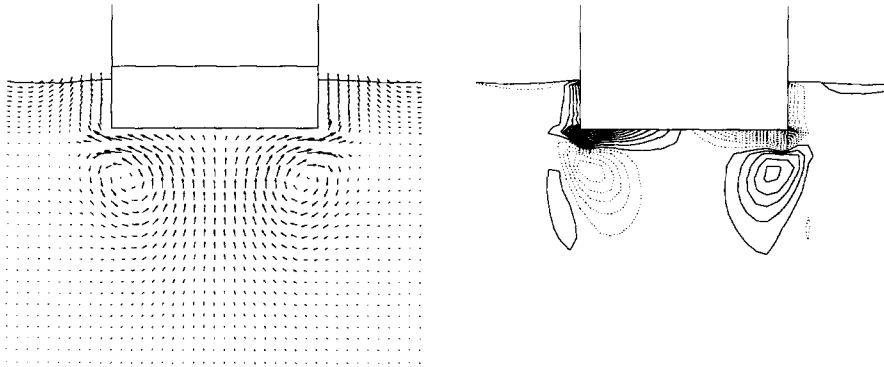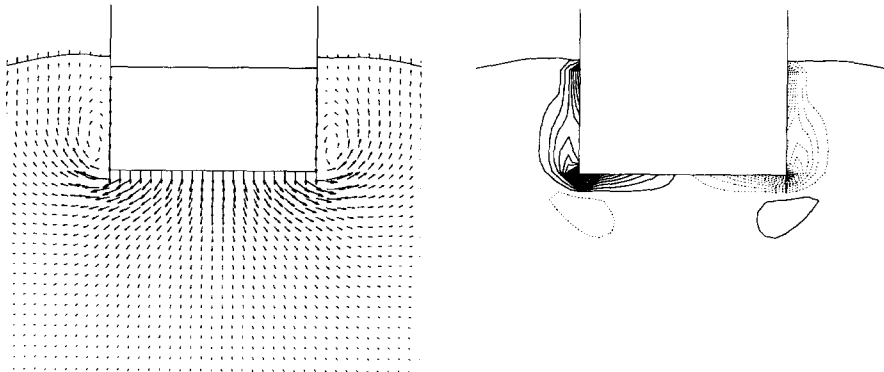
Fig. 3a

Fig. 3b

Fig. 3c

Fig. 3. Velocity-vector and vorticity contour plots for $R_\sigma = 10^3$, $F_\sigma = 2.0$, $a/B = 0.2$, $d/B = 0.5$, at (a) $t = 0.999\hat{T}$, (b) $t = 1.247\hat{T}$, (c) $t = 1.499\hat{T}$, and (d) $t = 1.814\hat{T}$. $\hat{T}$ is the period of oscillation. In the velocity-vector plots, the horizontal line in the body denotes the calm water level. The solid lines in the vorticity-contour plots denote negative (clockwise) vorticity and dotted lines positive (counterclockwise) vorticity.
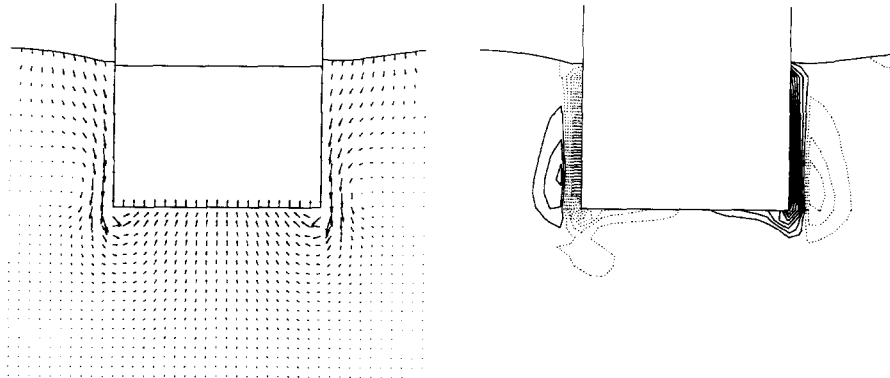
Fig. 3d

Fig. 3 (cont.).

diffusion while being convected downwards. The vorticity field is now dominant in the shear layer generated along the sides near the sharp edges. One can notice the formation of vortices in the side shear layers. Finally, in Fig. 3d, which corresponds to $t = 1.814\hat{T}$, the outward translation of the vortices formed earlier (in Fig. 3c) can be clearly seen. The primary flow at this time is again (as in Fig. 3a) into the bottom void as the body is ascending. In all of the above vorticity-contour plots, partial shedding of vorticity into the fluid can be observed.

4.2. Force calculations

First, heave-force components for a typical case ($d/B = 1.0$, $F_\sigma = 2.0$ and $a/B = 0.3$) are shown in Fig. 4. These shear-stress, viscous normal-stress, and dynamic-pressure components
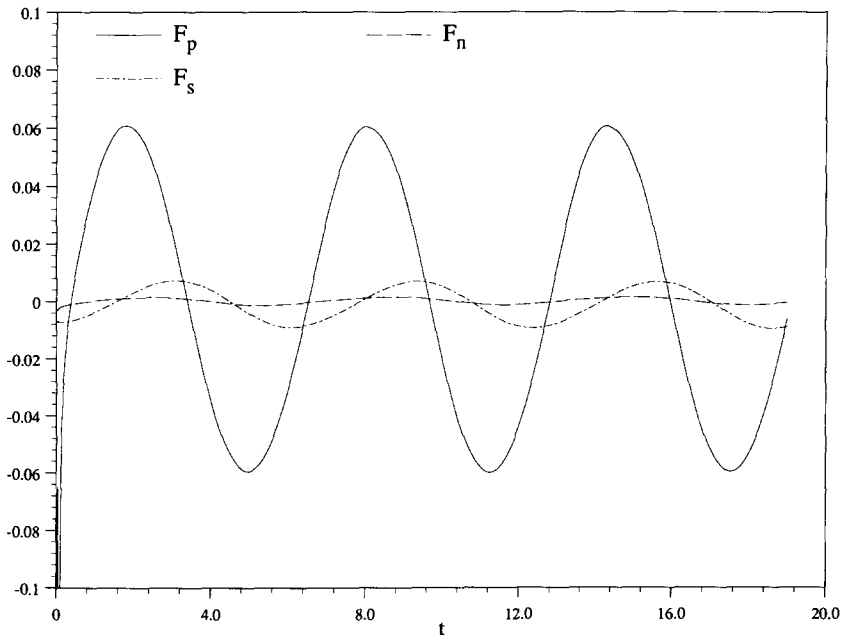

Fig. 4. Pressure and viscous-stress contributions to the heave force at $R_\sigma = 10^3$, $F_\sigma = 2.0$, $a/B = 0.3$, $d/B = 1.0$.

of the heave force are computed using equations (17) to (19). As can be observed in the figure, the pressure component is much larger than those of the viscous stress components. This is a well known fact for flows past bluff bodies with sharp edges. In the present case, the shear-stress contribution is about 10%, while that of the normal viscous stress is only about 1%, of the pressure force. The shear stress contribution will be even smaller at higher Reynolds-number flows. It should also be pointed out that the calculation of the shear stress requires a fine spatial resolution of the boundary layers. Because of the smallness of the viscous stress contribution, we will henceforth retain only the pressure term in the force computations.

In order to determine the influence of the amplitude and frequency of oscillation in the nonlinear heave forces, the following cases are studied:

$F_\sigma = 2.0$,   Case (i): $a/B = 0.1$,   Case (ii): $a/B = 0.2$;

$F_\sigma = 1.5$,   Case (iii): $a/B = 0.1$,   Case (iv): $a/B = 0.2$;

$F_\sigma = 1.0$,   Case (v): $a/B = 0.1$,   Case (vi): $a/B = 0.2$.

The draft-to-beam ratio d/B is set to be 0.5. Cases (i) & (ii) are presented in Fig. 5, (iii) & (iv) in Fig. 6, and (v) & (vi) in Fig. 7. The heave forces are normalized with respect to the amplitude of oscillation; i.e. presented as $F/(a/B)$, where F now is only the pressure component given by equation (19). The nonlinear viscous results are compared with those of linear, potential-flow, *frequency-domain*, steady-state results. The linear results are obtained using the solution method developed by Yeung in [33].

For purpose of reference, a *sine* curve $y(t) = 0.2 \sin t$, is drawn to indicate the position of the body. The value 0.2 is chosen merely for clarity.
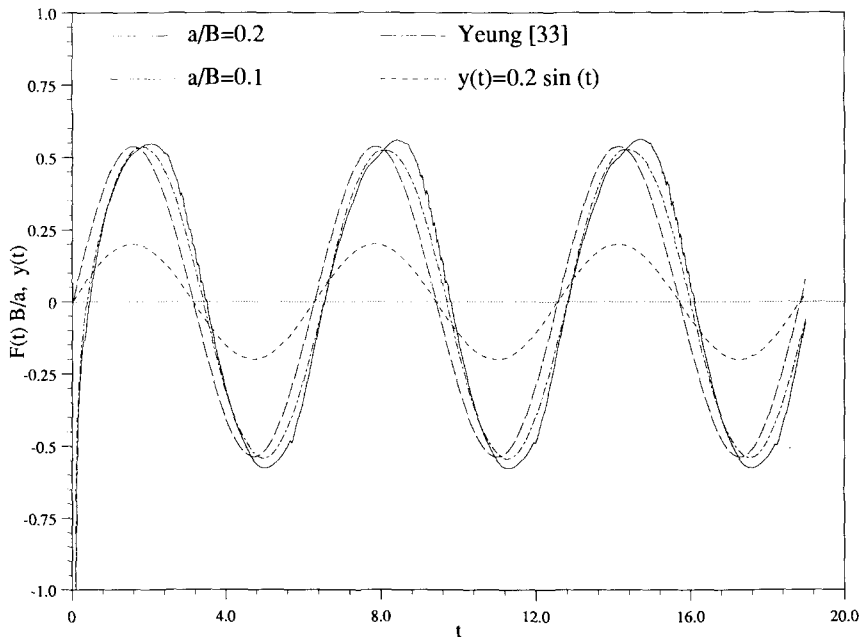

Fig. 5. Normalized viscous heave forces for $F_\sigma = 2.0$, $R_\sigma = 10^3$, $d/B = 0.5$ at amplitudes $a/B = 0.2$ and $a/B = 0.1$. For comparison, linear potential results (Yeung [33]) is given. Sine curve $y(t) = 0.2 \sin t$ indicates body position.
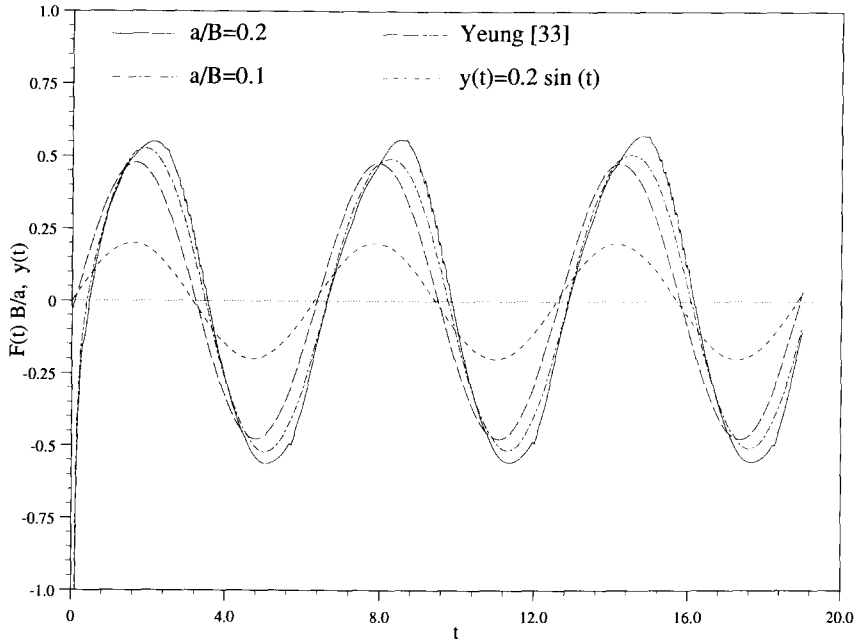
Fig. 6. Normalized viscous heave forces for $F_\sigma = 1.5$, $R_\sigma = 10^3$, $d/B = 0.5$ at amplitudes $a/B = 0.2$ and $a/B = 0.1$. For comparison, linear potential results (Yeung [33]) is given. Sine curve $y(t) = 0.2 \sin t$ indicates body position.
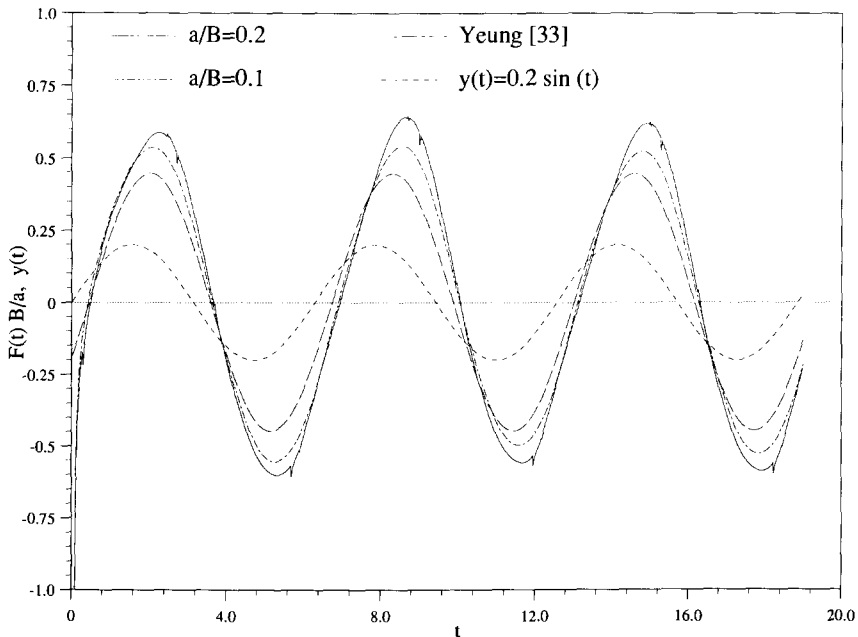

Fig. 7. Normalized viscous heave forces for $F_\sigma = 1.0$, $R_\sigma = 10^3$, $d/B = 0.5$ at amplitudes $a/B = 0.2$ and $a/B = 0.1$. For comparison, linear potential results (Yeung [33]) is given. Sine curve $y(t) = 0.2 \sin t$ indicates body position.

In all of the nonlinear viscous-flow calculations, negatively large values are found at the start of the simulation. Recall that the body motion is stated impulsively at $t = 0^+$. For such impulsively started motion in a viscous fluid, it has been shown that the stress on the body surface is square-root singular in t at $t = 0^+$ (see Bar-Lev and Yang [3]). However, this negatively large value seems to perpetuate only for a short duration of time.

Since the force curves are normalized with respect to the amplitude of oscillation, deviations in force curves of different a/B values would indicate nonlinear effects. Deviations of the computed results with respect to that of the linear, potential-flow theory is a measure of both nonlinear and viscosity effects. The phase shift of the force with respect to the body motion is attributed to the damping component (in phase with velocity) of the hydrodynamic forces.

Based on the results given in Figs 5–7, the following observations can be made:

- Inspection of results reveals that steady-state is reached within about two periods of oscillation.
- The negative phase shift of the linear potential force is small at $F_\sigma = 2.0$, since wave damping is almost negligible in this relatively high frequency regime (Fig. 5). However, it can be seen that the wave-damping component is quite large at the lower frequency $F_\sigma = 1.0$ of oscillation (Fig. 7).
- The phase shift is more negative (compared to linear potential results) in the case of nonlinear viscous solutions. It can also be observed, in general, that the phase shift increases with the increase in the amplitude of oscillation. This indicates the effect of viscosity on damping.
- In the high-frequency regime (e.g. Fig. 5), the amplitude of the computed viscous forces is close to that of the linear, potential-theory results when the amplitude of oscillation is small. This is consistent with the analytical results of Yeung and Wu [34]. It can also be observed that the negative peak of the force curve is larger in magnitude than that at the positive peak, a known nonlinear effect. The computed viscous forces deviate substantially from those of potential flow at low frequency (see Fig. 7).
- In general, the normalized heave forces are larger when the amplitude of oscillation is large. This increase is more dramatic at low frequency (Fig. 7).
- At large amplitude of oscillation, a rather uniform spiky behavior can be observed during the second quarter of the periodic motion (see Figs 5 and 6). During this interval, as shown in Figs 3b and 3c, eddies formed in the wake are convected and diffused, and the vortices at the sides near the sharp edges are also developing. It is believed that the spikes in the force results are caused by the drastic pressure changes accompanying the generation of these vortices at the edges. However, no such spiky pattern is observed at the smaller amplitude of oscillation.

Finally, to better elucidate the structure of the vorticity fields, we show in Fig. 8 a color plot of the vorticity contours corresponding to two different motion amplitudes ($a/B = 0.1$, 0.2). Both plots in this figure correspond to $d/B = 0.5$, $F_\sigma = 2.0$, and $t = 1.247\hat{T}$. Note that the contours are given in the computational space. The actual vortical structure in the physical space will be slightly distorted from these plots because of coordinate mapping. It can be seen that the intensity of the vorticity field is larger in the case of larger amplitude of oscillation. Vorticity generation at the free surface, because of its curvature, can also be seen in the case of large-amplitude motion.
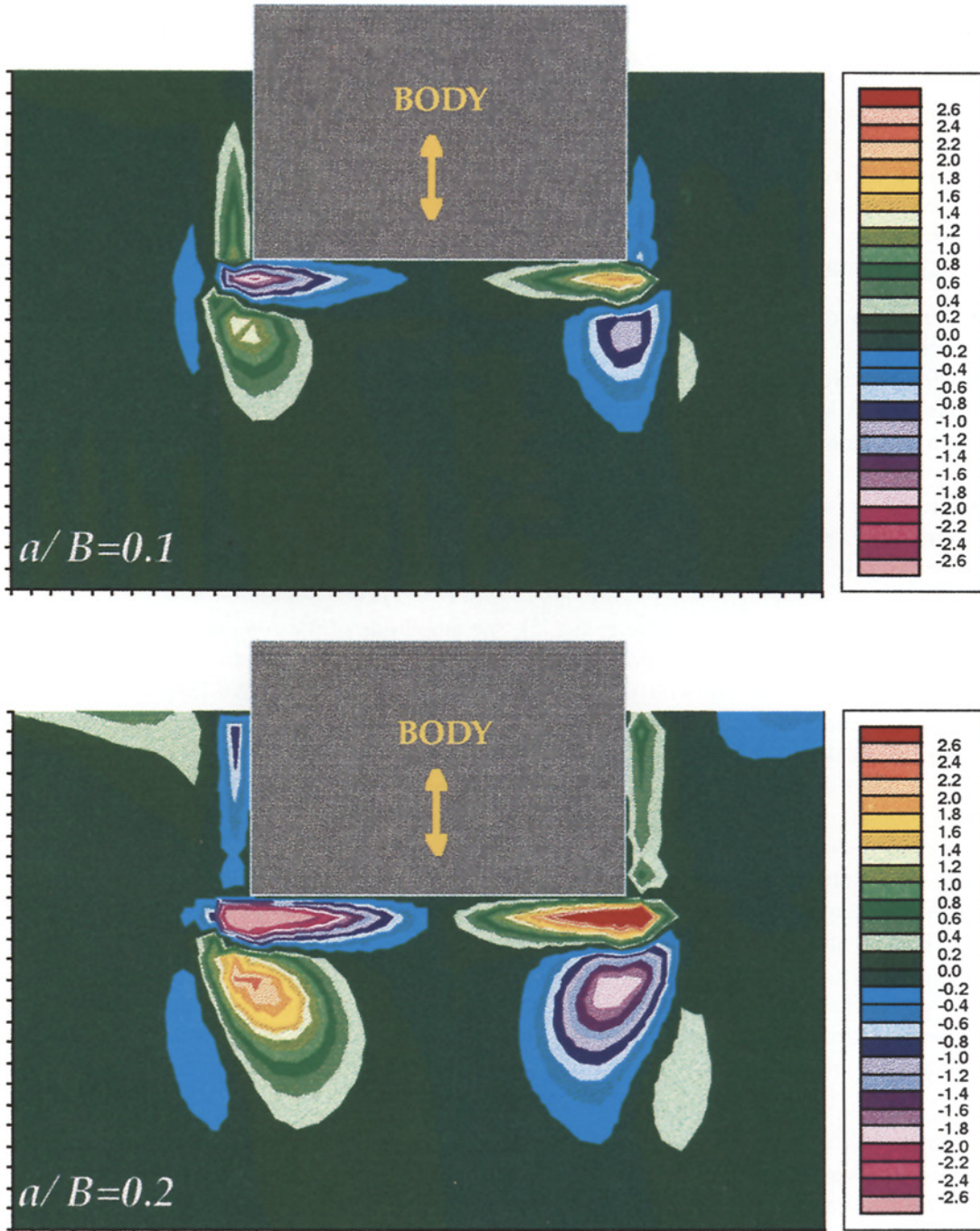
Fig. 8. Vorticity structure generated around cylinder, effects of amplitude of motion (shown in computational space); $F_\sigma = 2.0$, $R_\sigma = 10^3$, $d/B = 0.5$, and $a/B = 0.1$, $a/B = 0.2$. Positive contours (green and red spectrum) correspond to counterclockwise vorticity and negative contours (blue and pink spectrum) to clockwise vorticity.

5. Conclusions

A new method for the accurate solution of nonlinear, wave-body interaction problems in a viscous fluid has been developed. As has been shown in this paper, the present method is robust and is especially capable of coping with large amplitude of body oscillation. Although only heave motion is considered here, other modes of oscillation, such as sway and roll, or their combination, can be easily handled.

For the heave-motion study, we have provided some typical results corresponding to a fairly wide range of frequency and amplitude of heave motion. At high frequency, small-amplitude forces agree well with those of linear potential theory in magnitude. The difference in phase between the viscous and inviscid cases is due to viscosity effects. Nonlinear and quadratic-damping effects are clearly evident for the case of large amplitude of oscillation. At low frequency, it is shown that heave forces are strongly dependent on the amplitude of oscillation.

We were not able to provide results at extremely low frequencies, which would have required a very large numerical domain in order to avoid the ill effects of open-boundary reflections. Similar difficulty is also encountered in laboratory experiments because of tank-size limitations (see e.g. Vugts [26]). The scatter in the experimental data at low frequencies are customarily attributed to spurious effects of finite tank sizes. On the contrary, the results of Yeung and Wu [34], which were based on the linearized viscous-flow equations, show that viscosity effects could be important in the low-frequency regime in the laboratory scale. The present nonlinear work also seems to point towards that possibility. A more elaborate treatment of the open boundary is being developed. Once accomplished, we hope to resolve completely the precise role played by viscosity in the low-frequency regime.

Acknowledgement

References

1. P. Ananthakrishnan, *Surface waves generated by a translating two-dimensional body: effects of viscosity*. Ph.D. thesis, Department of Naval Architecture and Offshore Engineering, University of California at Berkeley, USA (1991).
2. G.B. Baker, D.I. Meiron and S.A. Orszag, Generalized vortex method for free-surface flow problems. *Journal of Fluid Mechanics* 123 (1982) 477–501.
3. M. Bar-Lev and H.T. Yang, Initial flow field over an impulsively started circular cylinder. *Journal of Fluid Mechanics* 72 (1975) 625–647.
4. J.T. Beale, Large-time regularity of viscous surface waves. *Archive for Rational Mechanics and Analysis* 84(4) (1984) 307–352.
5. J.B. Bell, P. Collela and H.M. Glaz, A second-order projection method for the incompressible Navier–Stokes equations. *Journal of Computational Physics* 85 (1989) 257–283.
6. J.U. Brackbill and J.S. Saltzman, Adaptive zoning for singular problems in two dimensions. *Journal of Computational Physics* 46 (1982) 342–368.

7. A.J. Chorin, Numerical solution of incompressible flow problems. *Studies in Numerical Analysis* 2 (1968) 64–71.
8. A.J. Chorin, Numerical solution of the Navier–Stokes equations. *Mathematics of Computations* 22 (1968) 745–762.
9. M.J. Cooker, D.H. Peregrine, C. Vidal and J.W. Dold, The interaction between a solitary wave and a submerged semicircular cylinder. *Journal of Fluid Mechanics* 215 (1990) 1–22.
10. E.B. Dussan V., The moving contact line: the slip boundary condition. *Journal of Fluid Mechanics* 77 (1976) 665–684.
11. M.A. Grosenbaugh and R.W. Yeung, Nonlinear free-surface flow at a two-dimensional bow. *Journal of Fluid Mechanics* 209 (1989) 57–75.
12. F.H. Harlow and J.E. Welch, Numerical calculation of time dependent viscous incompressible flow of fluid with free surface. *Physics of Fluids* 8 (1965) 2182–2183.
13. C. Hirsch, *Numerical Computation of Internal and External Flows I & II*. A Wiley-Interscience Publication (1988).
14. B.D. Nichols and C.W. Hirt, Methods for calculating multi-dimensional, transient, free surface flows past bodies. In *Proceedings*, First International Conference on Numerical Ship Hydrodynamics, Gaithersburg, Maryland (1975) 253–277.
15. C. Huh and S.G. Mason, The steady movement of a liquid meniscus in a capillary tube. *Journal of Fluid Mechanics* 81 (1977) 401–419.
16. J. Kim and P. Moin, Application of a fractional-step method to incompressible Navier–Stokes equations. *Journal of Computational Physics* 59 (1985) 308–323.
17. J. Koplik, J.R. Banavar and J.F. Willemsen, Molecular dynamics of fluid flow at solid surfaces. *Physics of Fluids A* 1(5) (1989) 781–794.
18. M.S. Longuet-Higgins and E.D. Cokelet, The deformation of steep surface waves on water: I. A numerical method of computation. *Proceedings, Royal Society of London* A350 (1976) 1–26.
19. H. Miyata, H. Kajitani, M. Zhu and T. Kawano, Nonlinear forces caused by breaking waves. In *Proceedings*, Sixteenth Symposium on Naval Hydrodynamics, Berkeley, California (1986) 514–536.
20. R.L. Potash, Second-order theory of oscillating cylinders. *Journal of Ship Research* 15(4) (1971) 295–324.
21. P.D. Sclavounos, Radiation and diffraction of second-order surface waves by floating bodies. *Journal of Fluid Mechanics* 196 (1988) 65–91.
22. S. Steinberg and P.J. Roache, Variational grid generation. *Numerical Methods in Partial Differential Equations* 2 (1986) 71–96.
23. R. Temam, *Navier–Stokes Equations – Theory and Numerical Analysis*. North-Holland Publishing Company (1979).
24. J.G. Telste, Calculation of fluid motion resulting from large-amplitude forced heave motion of a two-dimensional cylinder in a free surface. In: *Proceedings*, Fourth International Conference on Numerical Ship Hydrodynamics, Washington D.C. (1985).
25. T. Vinje and P. Brevig, Numerical simulation of breaking waves. *Advances in Water Resources* 4 (1981) 77–82.
26. J.H. Vugts, *The hydrodynamic coefficients for swaying, heaving, and rolling cylinders in a free surface*. Report No. 194, Laboratorium voor Scheepsbouwkunde, Technische Hogeschool, Delft, The Netherlands (1968).
27. J.V. Wehausen, The motion of floating bodies. *Annual Review of Fluid Mechanics* 3 (1971) 237–268.
28. R.W. Yeung and C-F. Wu, Nonlinear wave-body motion in a closed domain. *Computers and Fluids* 17 (1989) 351–370.
29. R.W. Yeung, Numerical methods in free-surface flows. *Annual Review of Fluid Mechanics* 14 (1982) 395–442.
30. R.W. Yeung and P. Ananthakrishnan, Solution of nonlinear water-wave and wave-body interaction problems using a new boundary-fitted coordinates method. In *Proceedings*, Fourth International Workshop on Water Waves and Floating Bodies, Øystese, Norway (1989) 269–274.
31. R.W. Yeung and P. Ananthakrishnan, Numerical grid generation for water-wave problems using reference space, *to be published* (1992).
32. R.W. Yeung and M. Vaidhyanathan, Nonlinear interaction of water waves with submerged obstacles, to appear in *International Journal on Numerical Methods in Fluids* (1992).
33. R.W. Yeung, A hybrid integral-equation method for the time-harmonic free-surface flows. In *Proceedings*, First International Conference on Numerical Ship Hydrodynamics, Gaithersburg, Maryland (1975) 581–608.
34. R.W. Yeung and C-F. Wu, Viscosity effects on the radiation hydrodynamics of horizontal cylinders. *Journal of Offshore Mechanics and Arctic Engineering* 113 (1991) 334–343.